



Estimating errors in vehicle secondary aerosol production factors due to oxidation flow reactor response time

Pauli Simonen¹, Miikka Dal Maso¹, Pinja Prauda¹, Anniina Hoilijoki¹, Anette Karppinen¹, Pekka Matilainen², Panu Karjalainen¹, and Jorma Keskinen¹

¹Aerosol Physics Laboratory, Physics Unit, Faculty of Engineering and Natural Sciences, Tampere University, Tampere, Finland

²Dinex Finland Oy, Vihtavuori, Finland

Correspondence: Pauli Simonen (pauli.simonen@tuni.fi)

Abstract. Oxidation flow reactors used in secondary aerosol research do not immediately respond to changes in the inlet concentration of precursor gases because of their broad transfer functions. This is an issue when measuring the vehicular secondary aerosol formation in transient driving cycles because the secondary aerosol measured at the oxidation flow reactor outlet does not correspond to the rapid changes in the exhaust flow rate. Since the secondary aerosol production factor is determined by multiplying the secondary aerosol mass with the exhaust flow rate, the misalignment between the two leads to incorrect production factors. This study evaluates the extent of the error in production factors due to oxidation flow reactor transfer functions by using synthetic and semi-synthetic exhaust emission data. It was found that the transfer function-related error could be eliminated when only the total production factor of full cycle was measured using constant volume sampling. For shorter segments within a driving cycle, a narrower transfer function led to smaller error. Even with a narrow transfer function, the oxidation flow reactor could report production factors that were more than 10 times higher than the true production factors if the segment duration was too short.

1 Introduction

Aerosol particles affect human health, climate and visibility (Pöschl, 2005; Seinfeld and Pandis, 2006). Organic compounds comprise approximately 20-90% of fine aerosol mass (Kanakidou et al., 2005), and a substantial fraction of organic aerosol originates from secondary aerosol formation (Zhang et al., 2007; Hallquist et al., 2009). The secondary organic aerosol (SOA) is formed in the atmosphere via oxidation of precursor gases. Resolving the total atmospheric SOA budget and the contributions from biogenic and anthropogenic sources is challenging, but it is estimated that the majority of SOA origins from biogenic sources. (Hallquist et al., 2009)

While SOA production from biogenic sources is globally higher than that of anthropogenic sources, the organic aerosol concentrations in large cities are dominated by anthropogenic SOA. High population density combined with local precursor emission sources results in significant contribution to air pollution mortality from anthropogenic SOA. (Nault et al., 2021) Nault et al. (2021) studied the health effects of anthropogenic SOA and used a set of aromatic precursor gases as a proxy for



total anthropogenic organic precursor emissions in selected cities. 20-62 m-% of these emissions originated from gasoline and diesel exhaust and fuel evaporation, which implies that vehicles are an important source of SOA in urban environments.

25 Vehicular SOA production is not currently directly regulated. Since SOA originates from gaseous organic compounds, limitations for hydrocarbon (HC) emissions indirectly limit SOA production but there is no universal constant to convert the measured HC emissions to potential SOA formation in the atmosphere. Thus, reduction of HC emission does not linearly translate to reduced SOA formation. Regulating the SOA production specifically would require measuring the SOA production factors (i.e., amount of potential SOA from emissions per fuel consumed) with smog chambers or oxidation flow reactors
30 (OFRs).

SOA production factors (PFs) from vehicles have been measured with smog chambers by driving a driving cycle and injecting the exhaust to the smog chamber during the cycle (e.g., Gordon et al. (2014a); Platt et al. (2013)). The chambers are typically operated in batch mode, so that the oxidation in the chamber is actuated after the driving cycle is finished. The advantage of smog chambers compared to oxidation flow reactors is that the oxidant concentrations are close to ambient levels so
35 that the photochemistry and aerosol processes resemble tropospheric conditions better. In contrast, the oxidant concentrations in OFRs are orders of magnitudes higher, which can introduce non-tropospheric effects (Peng and Jimenez, 2020). The OFRs are operated in continuous flow mode, which enables measurement of SOA production factors with good temporal resolution. Smog chamber experiments provide only the total SOA production factor of the driving cycle, while OFR measurements can resolve how the SOA production differs between different driving conditions within the driving cycle. However, the delay
40 caused by the residence time of the sample in the OFR complicates the calculation of SOA production factors. In this work, we address these complications.

While it is possible to measure HC and other pollutants directly from the tailpipe with only a small delay originating from the instrument response, the response time associated with a continuous SOA measurement using an OFR is significantly longer. Considering that potential SOA is always dependent on emitted HC to some extent, a natural first approach to address this issue
45 can be formulated as: How accurately could we estimate the HC emission by measuring HC at (non-oxidizing) flow reactor outlet instead of measuring directly from tailpipe?

When calculating the emission rates (g s^{-1}) or the total emission (g) of the exhaust gases, the gas concentrations in the tailpipe need to be multiplied with the exhaust flow rate. The total emission of gas C (in g) is calculated by

$$C_{emitted} = \int_{t_0}^{t_f} [C]_{true}(t) Q_{exh}(t) dt, \quad (1)$$

50 where t_0 and t_f are the start and end times of a driving cycle or event of interest, respectively, $[C]_{true}$ is the gas concentration (g m^{-3}) in tailpipe, Q_{exh} is the volumetric exhaust flow rate ($\text{m}^3 \text{s}^{-1}$) and the product of $[C]_{true}$ and Q_{exh} is the emission rate (g s^{-1}).

If the gas concentration (e.g. $[HC]$) is measured at the OFR outlet instead of the tailpipe, the emission rate and subsequently the total emission will be affected as illustrated in Fig. 1 (assuming that the OFR UV lamps are off so that none of the HC
55 will be oxidized). This is because the gas concentration is modified by the OFR residence time distribution (RTD): the gas

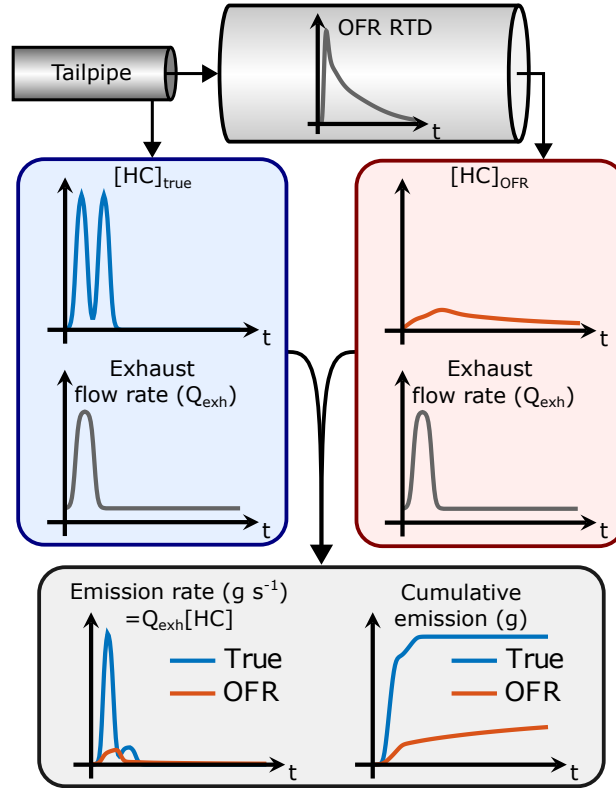


Figure 1. Determining HC emission by measuring HC concentration directly from tailpipe ($[HC]_{true}$) or downstream of an OFR ($[HC]_{OFR}$) and multiplying the concentrations with the engine exhaust flow rate (Q_{exh}). In this example, the OFR UV lamps are off so that none of the HC is oxidized. Even though the HC concentration at OFR outlet is lower because of OFR residence time distribution (RTD), the total integral is equal to that of the tailpipe HC concentration. However, the HC measured at OFR outlet will lead to underestimated HC emission because the area under OFR emission rate curve is smaller than the true area.

concentration at OFR outlet is result of convolution of the original gas concentration and the OFR transfer function, E . The transfer function is the RTD of a Dirac delta input impulse. (Fogler, 2006) Thus,

$$[C]_{OFR}(t) = ([C]_{true} * E)(t) = \int_0^t [C]_{true}(\tau) E(t - \tau) d\tau, \quad (2)$$

where $[C]_{OFR}$ is the gas concentration at OFR outlet (assuming no dilution) and $[C]_{true}$ is the concentration in tailpipe. As shown in Fig. 1, multiplication of $[C]_{OFR}$ with the exhaust flow rate does not lead to the correct emission when the exhaust flow rate is not constant. Determining the correct emission would require solving for $[C]_{true}$ from the OFR measurements. Even though the transfer function E can be determined, it is usually impossible to unambiguously solve for $[C]_{true}$ in Eq. 2 because this is an ill-posed inverse problem. Thus, it is not trivial to determine the SOA production factors from driving cycles with variable driving conditions where the exhaust flow rate is not constant.



65 Despite the difficulties in calculating SOA PFs with OFRs, this issue is not addressed in earlier publications (Karjalainen et al., 2016; Timonen et al., 2017; Simonen et al., 2019; Pieber et al., 2018; Zhang et al., 2023). Zhao et al. (2018) recognized the problem, but there is no analysis on the magnitude of error caused by the OFR transfer function. It is necessary to estimate how large an error is caused by OFRs with different transfer functions and to determine how to best account for the transfer function when analyzing the data.

70 Similar issues have been studied for situations where the exhaust system, sampling lines and non-ideal instrument response cause delay and distortion to exhaust gas or particle measurements (Ganesan and Clark, 2001; Ajtay and Weilenmann, 2004; Hawley et al., 2003; Weilenmann et al., 2003; Madireddy and Clark, 2006; Geivanidis and Samaras, 2007; Franco, 2014; Giechaskiel et al., 2021). Mahadevan et al. (2016) studied the error in gaseous emission factors in test cycles due to the phenomena mentioned above. They found that the error could be as high as 51% when using non-corrected data, and 25%
75 after applying a constant time shift to correct for the delay. The effect of delay and distortion is significantly higher for OFRs because their their dynamic response is much slower than that of gas analyzers or transportation lines.

In this study, we first present the theoretical background for calculating the SOA PF of vehicles running a transient driving cycle. Second, we study the OFR response in two real driving cycles and compare different measurement and data analysis methods. Third, we use synthetic data to further evaluate the performance of different OFRs and data analysis methods. Finally,
80 we suggest best practices when measuring SOA PF with OFRs and provide computational tools to test the performance of any OFR for which the transfer function is known.

2 Theoretical background

The SOA PF defines the amount of SOA that would be formed in the atmosphere from the emitted SOA precursor gases, normalized to e.g. fuel consumed or distance travelled. Thus, the fuel-specific SOA PF ($\text{mg kg}_{\text{fuel}}^{-1}$) can be defined as:

$$85 \quad SOA \text{ PF} = \frac{SOA}{\text{fuel consumed}} = \frac{SOA}{\text{emitted carbon}} \cdot k' = \frac{SOA}{C_{CO_2} + C_{CO} + C_{HC} + C_{PM}} \cdot k', \quad (3)$$

where SOA is the SOA formation potential (mg), i.e., the SOA that could be formed in the atmosphere from the emitted precursor gases. The emitted carbon is the mass of carbon emitted (g), which is the sum of emitted carbon mass originating from different exhaust compounds (CO_2 , CO , HC and particle phase carbon, C_{PM}) (Platt et al., 2013). The fuel consumed can be obtained from vehicle OBD data or by dividing the emitted carbon mass with the fuel carbon content denoted by k'
90 (g kg^{-1}). Since the emitted carbon is dominated by CO_2 , it is a good approximation to neglect the other forms of carbon. For simplicity, the SOA PF in this study is defined as:

$$SOA \text{ PF} \cong \frac{SOA}{CO_2} \cdot k, \quad (4)$$

where CO_2 is the emitted carbon dioxide mass and $k = k' \cdot 44/12$, i.e., the emitted CO_2 mass is multiplied with the ratio of carbon mass to total molecular mass in a CO_2 molecule.



95 To study the ability of OFRs to determine the SOA PFs, we use a simple model for SOA formation in which we assume that the potential SOA is directly proportional to emitted hydrocarbon mass (HC), i.e.

$$SOA = Y \cdot HC, \quad (5)$$

where Y is the proportionality factor. We assume that the factor Y for the OFRs and for the environmental chamber equals the value of Y in the atmosphere, and that Y is constant (independent of driving conditions). Thus, the total SOA formation
100 potential for time interval $[t_0, t_f]$ in a driving cycle is:

$$SOA_{true} = \int_{t_0}^{t_f} [HC]_{true}(t) \cdot Y \cdot Q_{exh}(t) dt, \quad (6)$$

where $[HC]_{true}$ is the mass concentration of gaseous hydrocarbons (mg m^{-3}) in the tailpipe and Q_{exh} is the exhaust gas volumetric flow rate ($\text{m}^3 \text{s}^{-1}$).

To simplify the analysis, we treat the product of momentary HC concentration and the proportionality factor Y as a theoretical SOA concentration ($[SOA]$) in the tailpipe, which reflects the potential of exhaust to form SOA in the atmosphere.
105 Hereafter, the term 'true SOA concentration' refers to HC concentration in the tailpipe multiplied with Y , and 'SOA emission' refers to SOA formation potential from emitted HC as defined in Eq. 5. In the OFR results, the SOA concentration is the simulated concentration of SOA measured at OFR outlet (HC concentration at OFR outlet multiplied with Y).

2.1 Determining SOA PF with an OFR

110 As shown in Fig. 1, the HC emission determined from HC concentration measurement at OFR outlet differs from the true HC emission. If the potential SOA formation is dependent on HC emission as shown in Eq. 5, a similar error is present when measuring the SOA emission with an OFR. The HC signal at the OFR outlet is delayed because of the residence time in the OFR but also distorted because of the residence time distribution as shown in Eq. 2. Ideally, the true HC (or SOA) emission could be resolved from OFR measurements by deconvolution, but the noise present in the measurement prevents a perfect
115 deconvolution of Eq. 2. Even without the noise, it is possible that no unique solution to the inversion problem exists. Thus, it is necessary to evaluate alternative methods to estimate SOA production factor based on the distorted OFR signal.

The delay caused by the OFR can be addressed by shifting the OFR signal with a characteristic time constant of the OFR:

$$[C]'_{OFR}(t) = [C]_{OFR}(t + \tau), \quad (7)$$

where $[C]_{OFR}$ is the concentration measured downstream of the OFR and $[C]'_{OFR}$ is the delay corrected concentration. The
120 constant τ is a characteristic delay of the OFR, which will be discussed in Sect. 5.1. The HC concentration at OFR outlet shown in Fig. 1 is already delay corrected, so that the peak concentration at OFR outlet is approximately aligned with the tailpipe peak concentration. Note that this delay correction requires that the OFR start sampling zero air immediately after the cycle ends, and that the measurement downstream of OFR be continued for at least duration of τ for the delay corrected OFR measurement to cover the full driving cycle.



125 By applying the delay correction to OFR data, the SOA emission in OFR measurement is

$$SOA_{OFR} = \int_{t_0}^{t_f} [SOA]'_{OFR}(t) \cdot Q_{exh}(t) dt \quad (8)$$

$$= \int_{t_0}^{t_f} [HC]'_{OFR}(t) \cdot Y \cdot Q_{exh}(t) dt, \quad (9)$$

where $[HC]'_{OFR}$ is the delay-corrected HC concentration measured at OFR outlet that is affected by the OFR transfer function as shown in Eq. 2. Note that $[SOA]_{OFR}$ is the quantity that is measured in OFR experiments, and the $[HC]_{OFR}$ is the HC concentration that would be measured at OFR outlet only if there was no oxidation in the OFR. In normal experiments where the OFR UV lamps are switched on, Eq. 9 does not hold since part of HC is transformed to particle phase. Here the non-oxidised HC concentration is only used to simulate the theoretical SOA concentration at OFR outlet. Additionally, the exhaust sample is normally diluted before introducing it to the OFR but in this study we assume no dilution. Applying a constant dilution factor does not change the results of the analysis.

135 Comparison of Eqs. 8 and 6 shows that SOA_{OFR} is unequal to true SOA emission because the delay correction does not correct for the distortion inside the OFR (Eq. 2), which leads to misalignment between exhaust flow rate and $[HC]_{OFR}$. The only case where SOA_{OFR} universally equals true emitted SOA is when the OFR transfer function is a Dirac delta function, i.e., when the OFR is an ideal plug-flow reactor.

For a full driving cycle, it is possible to avoid the mismatch between Q_{exh} and the SOA measured with an OFR by using a constant volume sampler (CVS), like e.g. Zhao et al. (2018), Kuittinen et al. (2021a, b) and Park et al. (2021) did. In a CVS, the exhaust is diluted with dilution ratio (DR) that is inversely proportional to the exhaust flow rate:

$$DR_{CVS}(t) = \frac{Q_{CVS}}{Q_{exh}(t)}, \quad (10)$$

where Q_{CVS} is the constant volumetric flow rate of the CVS. CVS should also be used in smog chamber experiments (e.g., Gordon et al. (2014a, b); Roth et al. (2020)); otherwise the injection of the exhaust into the smog chamber will not be proportional to the exhaust flow rate, i.e., the actual emission to the atmosphere.



When an OFR is sampling downstream of CVS, the true SOA emission is obtained with an OFR despite its transfer function by multiplying the SOA concentration at OFR outlet with the CVS flow rate and integrating over the full cycle:

$$\int_{t_0}^{t_f} [SOA]_{OFR}(t) \cdot Q_{CVS} dt = \int_{t_0}^{t_f} [HC]_{OFR}(t) \cdot Y \cdot Q_{CVS} dt = Q_{CVS} \int_{t_0}^{t_f} \left(\frac{[HC]_{true} \cdot Y}{DR_{CVS}} * E \right) (t) dt \quad (11)$$

$$= Q_{CVS} \int_{t_0}^{t_f} \left(\frac{[HC]_{true} \cdot Y \cdot Q_{exh}}{Q_{CVS}} * E \right) (t) dt = \int_{t_0}^{t_f} ([HC]_{true} \cdot Y \cdot Q_{exh} * E) (t) dt \quad (12)$$

$$150 = \int_{t_0}^{t_f} [HC]_{true}(t) \cdot Y \cdot Q_{exh}(t) dt \cdot \int_{t_0}^{t_f} E(t) dt, \quad t_0 = 0, t_f \rightarrow \infty \quad (13)$$

$$= \int_{t_0}^{t_f} [HC]_{true}(t) \cdot Y \cdot Q_{exh}(t) dt = SOA_{true}, \quad t_0 = 0, t_f \rightarrow \infty. \quad (14)$$

The separation of the convolution in Eq. 13 requires that the limits of integration be for the full defined range, i.e., $t_0 = 0$ and $t_f \rightarrow \infty$, as this is the full range of E (Weisstein, 2023). In this case also the integral of E is cancelled since it is unity by definition (and when dividing with emitted CO_2 to obtain the SOA PF, also Q_{CVS} in Eq. 11 is cancelled). Thus, by using
 155 CVS it is possible to obtain the true SOA PF for the full cycle but not for parts of it. This issue was noticed also by Zhao et al. (2018) when determining the PFs for different phases of a driving cycle. In practice, t_f does not need to be infinite, but it should extend beyond the end of the driving cycle to account for the residence time in the reactor, and for this reason also the measurement of $[SOA]_{OFR}$ should be continued after the end of the driving cycle and zero air should be injected to the reactor during that time. For the driving cycles and OFRs studied here, the error in full cycle PF is less than 5% when using
 160 CVS sampling where the post-sampling duration is equal to OFR mean residence time, and the error approaches zero with longer post-sampling time (Fig. S13).

The advantage of OFRs is the continuous measurement to study the effect of different driving conditions on SOA formation. Thus, even though the CVS is a good solution for measuring the full cycle SOA PF, the applicability of OFRs for time resolved vehicular SOA studies remain unclear. The extent of the error in measured SOA emission caused by the distortion will be
 165 studied for different scenarios in the following sections by simulating direct sampling from the tailpipe and using Eq. 8, and by simulating CVS sampling and using Eq. 11 where the integration range is significantly shorter than the full cycle length.

3 Results and discussion

To study the effect of OFR RTD on the accuracy of SOA production factor, we simulate the SOA concentration at OFR outlet for two OFRs that have distinct residence time characteristics. The Potential aerosol mass (PAM) reactor (Lambe et al., 2011)
 170 represents an OFR with a broad transfer function, with mean residence time of 142 s and transfer function standard deviation of 113 s. A prototype version of Dekati oxidation flow reactor (DOFR; Dekati Ltd) has a faster response with mean residence



time of 41 s and transfer function standard deviation of 21 s. All OFR data shown hereafter is delay corrected according to Eq. 7 with the peak residence time of the OFR (see Sect. 5.1).

3.1 Real driving cycles

175 We measured the HC and CO₂ concentrations in the exhaust of a Euro 6 gasoline vehicle running two driving cycles to obtain reference data. In this analysis, we assume that the measured HC and CO₂ values represent the true concentrations in the exhaust. The driving cycles were cold-start (CS) New European driving cycle (NEDC) which was preceded by soaking time of 15 h and started with an engine start, and hot-start (HS) NEDC which was preceded by driving at 80 km h⁻¹ speed for 5 min and started with an idling engine.

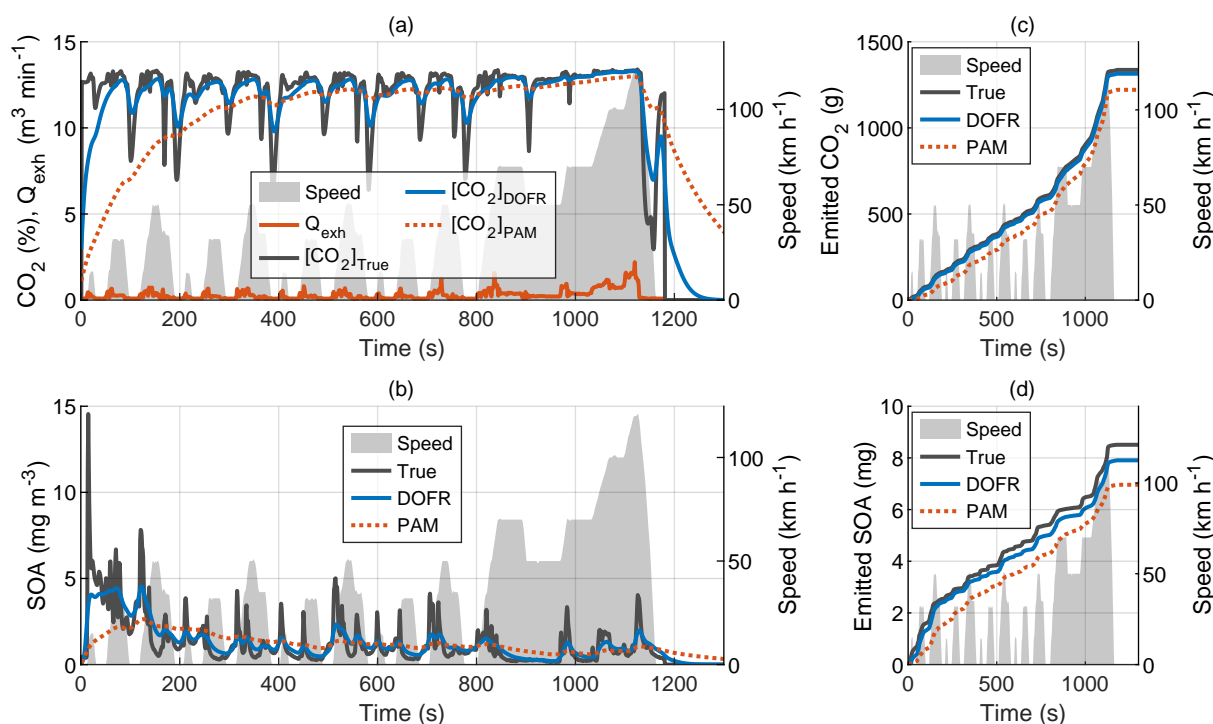


Figure 2. Time series of exhaust flow rate (Q_{exh}), tailpipe and OFR outlet concentrations of CO₂ (a) and SOA (b) in hot-start NEDC, and the cumulative emissions of CO₂ (c) and SOA (d). The OFR data is simulated based on tailpipe concentrations and OFR transfer functions, and the SOA concentration refers to HC concentration multiplied with Y . All OFR data is delay corrected.

180 It is currently not possible to determine a true reference for the SOA formation potential so we generated semi-synthetic data based on the measured HC concentration and the assumption that SOA formation potential is directly proportional to the HC emission (Eq. 5). The proportionality factor of 0.15 was used, resulting in realistic SOA PFs of approximately 100 and 20 mg kg_{fuel}⁻¹ for cold-start and hot-start cycles, respectively. The gas concentrations (and SOA concentration) at OFR outlets were simulated by convolving the tailpipe concentrations with the OFR transfer functions (Eq. 2). We assumed that the reactors



185 were sampling zero air until the cycle starts; otherwise, the exhaust from preceding driving would be present in the OFRs and affect the cycle-specific SOA PF.

Figure 2 shows the CO_2 concentrations and SOA concentrations, and their cumulative emissions in the hot-start NEDC. Similar graphs for the cold-start NEDC are shown in Fig. S2. The SOA concentration at the DOFR outlet follows the true SOA concentration better than PAM, which results in better agreement on the total emitted SOA at the end of the driving cycle (Fig. 190 2d). However, the DOFR-based total SOA emission is still 7% lower than the true SOA emission, mainly because the response is not fast enough to follow the true SOA concentration during accelerations where the exhaust flow rate is highest. PAM has the same effect, but in addition the PAM-derived SOA emission starts to deviate from the true SOA emission already in the beginning of the cycle because the response is too slow to catch the SOA peak in the cycle start. These two effects result in total SOA emission that is 18% lower than the true SOA emission.

195 Because the SOA PF is directly proportional to ratio of emitted SOA and emitted CO_2 , the relative error in PF equals the relative error in the SOA emission. However, for the OFRs both SOA emission and CO_2 emission (calculated from the delay corrected CO_2 measured at OFR outlet) are underestimated in the driving cycles studied here, so the error in PF could be decreased by normalizing the SOA emission to CO_2 emission measured at OFR outlet instead of true CO_2 emission. Even though this calculation method leads to better estimation of SOA PF in the two cases studied here, it is not guaranteed that the error in CO_2 measurement will always compensate for the error in SOA measurement. It is possible that in some cases the SOA emission determined from OFR measurements is higher than the true emission, and in such case normalizing to OFR CO_2 would amplify the error. Therefore, when presenting the integrated SOA PFs (e.g. Fig. 3a), the SOA emission is normalized to true CO_2 emission. 200

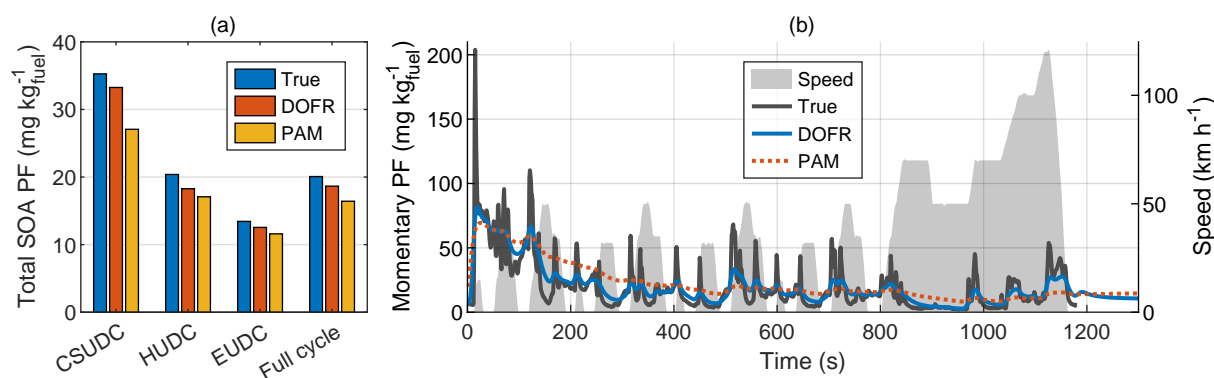


Figure 3. Total SOA PFs of subcycles and full driving cycle (a), and time series of true SOA PF and SOA PFs determined from OFR outlet concentrations (b) in hot-start NEDC. The integrated SOA PF in panel (a) is calculated by normalizing the SOA emission to true CO_2 emission, whereas for the momentary SOA PF in panel (b), the SOA concentration is normalized to OFR CO_2 concentration. The PFs in both panels are calculated from semi-synthetic SOA data that is linearly proportional to the measured HC concentration in the tailpipe or the simulated HC at OFR outlet. CSUDC, HUDC and EUDC represent approximately 400 s subcycles within the full cycle.



The error in full cycle SOA PFs is relatively small for both cold- and hot-start driving cycles despite the distorting effect of OFR transfer functions. In hot-start NEDC, the error in total SOA PF is 7% for DOFR and 18% for PAM (Fig. 3), and in cold-start NEDC the corresponding errors are 4% and 7% (Fig. S3). To study the accuracy of SOA PF in smaller subcycles, we divided the NEDC into three parts according to Karjalainen et al. (2016): cold start urban driving cycle (CSUDC; 0...391 s), hot urban driving cycle (HUDC; 392...787 s) and extra-urban driving cycle (EUDC; 788...1180 s). The division is used here also for the hot-start cycle although the term CSUDC does not represent a cold start in that case. The maximum error in the subcycles was 10% for DOFR (hot-start HUDC) and 23% for PAM (hot-start CSUDC). Note that the SOA PFs for the subcycles (Fig. 3a) are not the average values of momentary PFs shown in Fig. 3b. Instead, the subcycle SOA PF is calculated by normalizing the SOA emitted during the subcycle to the emitted CO₂.

The continuous operation of the OFRs allows studying SOA production factors at higher time resolution than the ~400 s subcycles. Zhang et al. (2023) investigated SOA PF as a function of driving condition by using a fast-response OFR (Veh-OFR). Such analysis requires time resolution in order of seconds, and the effect of OFR transfer function on the accuracy of momentary SOA PF at such time resolution needs to be determined.

The time-resolved true and OFR SOA PFs are shown in Fig. 3b for hot-start driving cycle and in Fig. S3b for cold-start driving cycle. The time-resolved OFR SOA PFs were calculated by normalizing the SOA concentration to CO₂ measured at OFR outlet to compensate for the slow response in SOA measurement. This is important especially in the beginning of the cycle, where the CO₂ levels in the OFRs deviate significantly from the tailpipe concentration.

Figure 3b shows that although the DOFR PF time series resembles better the true PF time series than PAM, neither of the OFRs can follow the rapid changes of the true SOA PF. For example, the maximum OFR PFs during the acceleration starting at 313 s are approximately 40% of the true maximum PF. However, when integrating the SOA and CO₂ emissions for a longer time interval, the agreement between the true PF and OFR PFs improves. For the full duration of the acceleration (313...343 s), the DOFR PF is 74% and PAM PF is 82% of true PF. In general, the longer the integration time interval, the better the agreement (Fig. S11). Thus, when studying the effect of driving conditions on SOA production, it is better to divide the driving cycle in bins that represent different driving conditions instead of determining the relations based on second-by-second data.

To study the accuracy of different OFRs, we divide the driving cycle in short events according to different driving conditions: accelerations, constant speed driving, idling and decelerations. The time periods are shown in Fig. S14, and the deviations from the true SOA PF for each driving condition are shown in Fig. 4. The corresponding correlation graphs are shown in Fig. S15.

Figure 4 shows that DOFR with narrower RTD is generally better suitable for studying SOA PFs of short events than PAM. In the cold-start cycle, PAM typically overestimates the PF because the HC originating from the engine start remain in PAM for a long time. In both cycles, the acceleration PFs are usually underestimated by both OFRs because there is typically simultaneous increase in exhaust flow rate and HC concentration, but the OFR HC does not reach the level of true HC as illustrated in Fig. 1. In constant-speed driving, both OFRs overestimate SOA PF because this driving condition is usually preceded by accelerations, and HC originating from the acceleration is still present in the OFRs. For the same reason, the OFRs overestimate also the deceleration PFs.

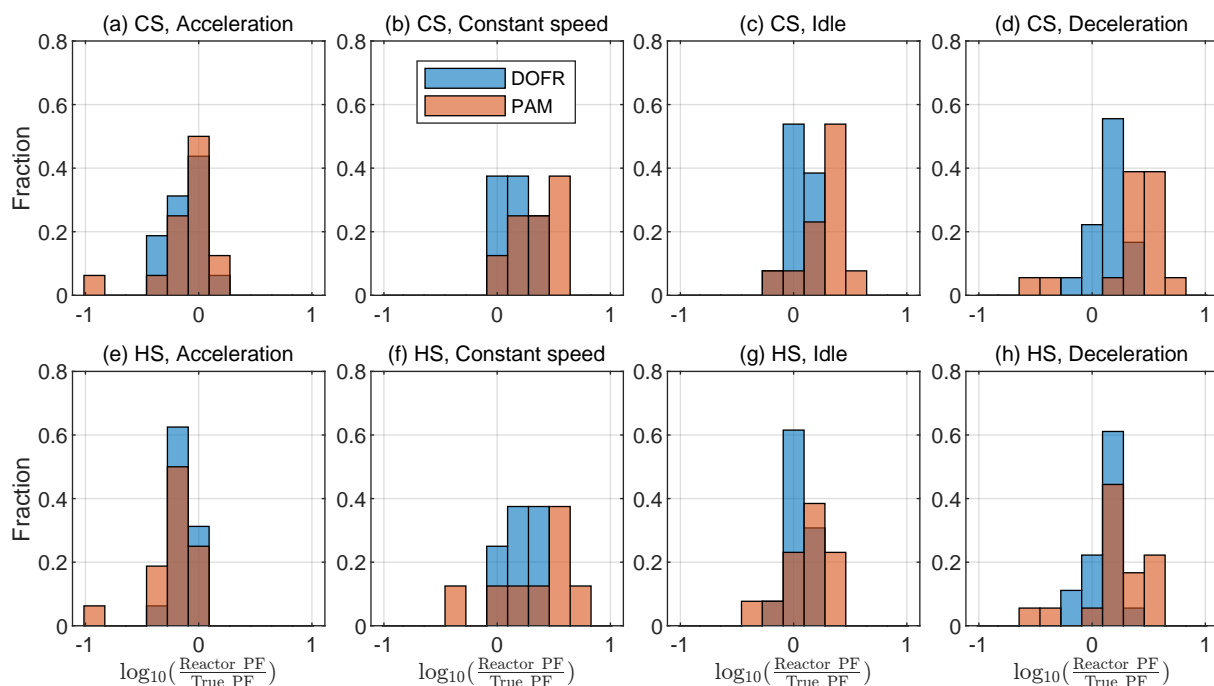


Figure 4. OFR SOA PF deviation from true PF for different driving condition bins, when the SOA PF is determined by normalizing the emitted SOA to true emitted CO_2 . The cold-start cycle is denoted as CS and hot-start as HS. Corresponding correlation plots are shown in Fig. S15. The PFs are calculated from semi-synthetic SOA data that is linearly proportional to the measured HC concentration in the tailpipe or the simulated HC at OFR outlet.

As discussed earlier, normalizing the emitted SOA to CO_2 emission determined from CO_2 concentration measured at OFR outlet may reduce the error in SOA PF. The applicability of this method and other methods to reconcile the distortion in SOA concentration caused by the OFR transfer functions are studied in the next section.

3.1.1 Alternative data analysis and measurement methods

Figure 5 shows the SOA PF deviations for both reactors when using different data analysis and measurement methods. Overall, the different methods (except for the averaging method) result in relatively small error, maximum 37 %. In all methods, the OFR data is delay corrected.

The **standard method** is the one used in previous sections, i.e., the SOA emission is normalized to true CO_2 emission. This method underestimates the SOA PF in most cases (Fig. 5). Note that normalization to true CO_2 emission is equivalent to normalizing to true fuel consumed or true distance travelled. When using the other data analysis methods described below and calculating the distance based production factors, one first needs to determine the fuel-specific production factor and only then convert it to distance based by multiplying with the ratio of fuel consumed per distance travelled that is available in the on-board diagnostics data.

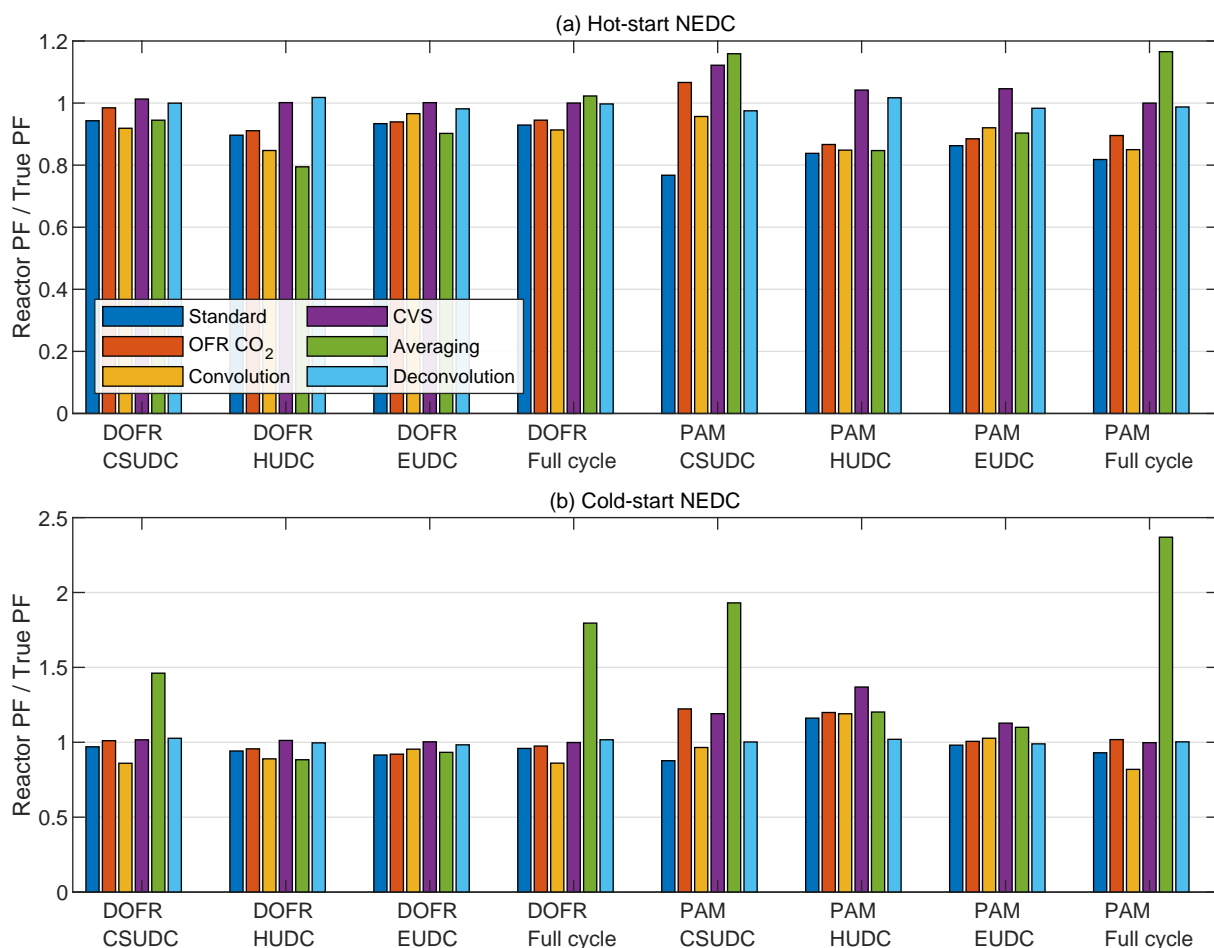


Figure 5. OFR SOA PF deviation from the true PF for full driving cycles and ~400 s subcycles when using different data analysis and measurement methods. The PFs are calculated from semi-synthetic SOA data that is linearly proportional to the measured HC concentration in the tailpipe or the simulated HC at OFR outlet.

In the **OFR CO₂ method** the CO₂ concentration is measured from OFR outlet and the CO₂ emission is determined by multiplying the delay-corrected CO₂ concentration with the exhaust flow rate. In most cases, the **OFR CO₂** method results in better agreement with the true SOA PF compared to standard method (Fig. 5), which is in agreement with the observation that both SOA and CO₂ emissions are underestimated with the OFR in Fig. 2.

255 The **convolution method** applies the same OFR response to the exhaust flow rate that affects the SOA and CO₂ concentrations that are measured at OFR outlet. The SOA and CO₂ emission rates are calculated by multiplying the concentrations at OFR outlet with exhaust flow rate that is convolved with OFR transfer function. This method was used by Simonen et al. (2019) for determining SOA emission rate, but it was not normalized to CO₂ emission measured at the OFR outlet but to the



true fuel consumption or distance travelled, which is equal to normalizing to true CO₂ emission. The deviation in *convolution*
260 method is of similar magnitude to the standard method and the *OFR CO₂* method (Fig. 5).

In the **CVS method**, the OFRs are sampling exhaust that is diluted with CVS, i.e., the dilution ratio is inversely proportional
to the exhaust flow rate. The emitted SOA is calculated with Eq. 11. The emitted CO₂ is calculated with a similar equation,
where the CO₂ is measured at the OFR outlet. The CVS method always leads to correct SOA PF for the full cycle as discussed
in Sect. 2.1. For DOFR, the CVS method results in least deviation in subcycles as well compared to the methods presented
265 above. For PAM, the deviation in subcycles with this method is on average larger than the previous methods in cold-start cycle,
but performs better in the hot-start cycle.

Although the CVS sampling is favorable especially for DOFR, it has some disadvantages. CVS requires a high flow rate
of dilution air compared to partial flow diluters, and purifying such amounts of dilution air is challenging. This may lead to
high background SOA formation from dilution air impurities (Zhao et al., 2018). In addition, the heat from vehicle exhaust
270 may cause desorption of previously adsorbed HC from CVS walls (Gordon et al., 2014a). However, the SOA PFs have been
measured with CVS sampling with acceptable background SOA formation (Zhao et al., 2018; Kuittinen et al., 2021a; Gordon
et al., 2014a).

An inherent feature of the CVS is that the dilution ratio is inversely proportional to exhaust flow rate. As shown in Fig. 2,
the HC peaks usually occur during accelerations, where the exhaust flow rate is also elevated. The same is observed for NO_x,
275 so the use of CVS dilution amplifies the variations in HC and NO_x concentrations compared to direct sampling from tailpipe
with constant dilution ratio. Since the OH exposure and photochemistry in OFRs is sensitive to concentrations of NO_x and OH
reactive gases (Peng and Jimenez, 2017), using CVS may cause too high gas concentrations during e.g. accelerations where
exhaust flow rate and gas concentrations are high, and too low signal during e.g. idling where concentrations and exhaust flow
rate are low.

The **averaging method** does not consider the exhaust flow rate. In the study by Zhang et al. (2023), the full cycle SOA PFs
280 were apparently determined by calculating the average of the momentary PFs instead of calculating the ratio of emitted SOA
to emitted CO₂, although their description of the PF calculation for full cycle is not unambiguous. Figure 5 shows that in the
cold-start cycle, this *averaging* method leads to an overestimation by a factor of ~ 2 for DOFR and ~ 2.5 for PAM. Note that
the PFs calculated with the *averaging* method are not compared to the average values of true momentary PFs, but instead to
285 the true PF which is the emitted SOA normalized to emitted CO₂.

In the **deconvolution method**, the SOA signal simulated at OFR outlet is first deconvolved (as described by Conesa (2020);
see Sect. S2) to obtain the true SOA concentration in tailpipe, and then multiplied with true exhaust flow rate to obtain the
SOA emission rate. The emitted SOA is normalized to true emitted CO₂. For PAM, the *deconvolution* method leads to smallest
errors, whereas for DOFR the CVS method is as good as the *deconvolution* method. The time series of deconvolved SOA
290 concentrations are shown in Fig. S16.

The deconvolution here represents the best possible outcome because there is no noise present in the simulated SOA concen-
tration at OFR outlet. In real-life scenarios, there is noise originating from the instrument measuring the SOA concentration and
also some variability in the OFR transfer functions due to small fluctuations in flow rate and temperature. The performance of

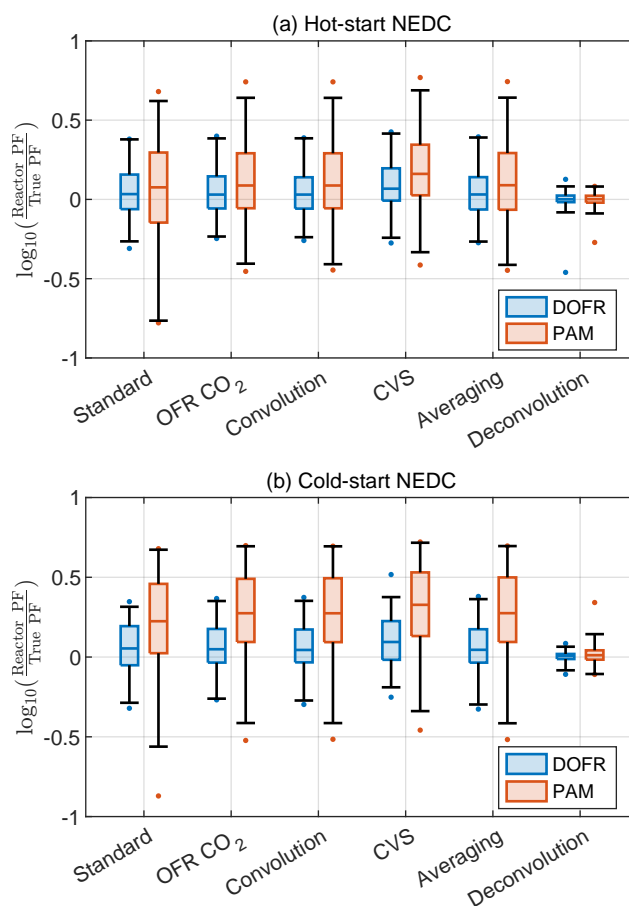


Figure 6. The deviation of OFR PFs for 14 s bins in the driving cycles when using different data analysis and measurement methods. Boxes represent 25th and 75th percentiles, and the line inside the box represents the median value. The points are considered outliers if they are greater than 99th percentile or lower than 1st percentile. The whiskers extend to most extreme data points that are not outliers. The PFs are calculated from semi-synthetic SOA data that is linearly proportional to the measured HC concentration in the tailpipe or the simulated HC at OFR outlet.

the *deconvolution* method in such cases is beyond the scope of this study, but our tests for 10 s square pulses of SOA precursor showed that the deconvolution was able to reproduce the square pulses based on the measured SOA concentration at DOFR outlet, but not perfectly (Fig. S9).

While all calculation methods except the *averaging* method are able to report the SOA PF for full cycles and ~ 400 s subcycles with relatively good accuracy, Fig. 4 shows that in some cases, the deviation in short driving events can be very high when using the *standard* method. Some of the deviations in Fig. 4 could be avoided by normalizing the SOA emission to the CO_2 measured at OFR outlet instead of tailpipe. For example, the most severe underestimations in PAM and DOFR are observed in the beginning of the driving cycles where the response to HC is much slower than the change in the tailpipe CO_2



concentration, and in other occasions where there is drastic change in tailpipe CO₂ concentration. Likewise, the changes in tailpipe CO₂ concentration during decelerations are much faster than the characteristic residence times of the OFRs. For this reason, we investigate whether the normalization to OFR CO₂ or any of the other methods perform better for short events in the driving cycles. For this analysis, we divide the cycle in 14 s bins and calculate the deviation from true PF for each bin using different methods. The 14 s bin duration was chosen because it is the median duration of different events in Fig. 4.

Figure 6 shows that different calculation methods, including the *averaging* method (but excluding the *deconvolution* method), report similar distributions for the deviations in short driving events. However, the *standard* method usually has more deviation at low values due to the CO₂ issue mentioned before. The *deconvolution* method is superior for both OFRs: 98% of all OFR data is within factors of 0.81 and 1.39 of true PF. Because of this high accuracy, the applicability of *deconvolution* method in real-world scenarios should be studied in a future publication.

Both reactors tend to overestimate the SOA PFs of short events. For example, in *OFR CO₂* method the median ratios between OFR PFs and true PFs are 1.08 and 1.13 for DOFR in hot- and cold-start cycles, respectively. For PAM, the median ratios are 1.24 and 1.87 in hot- and cold-start cycles, respectively, and in cold-start NEDC 75% of PAM PFs exceed the true PFs.

3.2 Special cases

Although the DOFR usually reports PFs closer to true values than PAM, this is not always the case. Figure 7 shows two synthetic examples: one where the HC concentration increases simultaneously with exhaust flow rate (typical acceleration observed in the driving cycles presented), and another where the peak in exhaust flow rate is not aligned with the HC concentration peak (e.g., a HC peak originating from engine start followed by elevated exhaust flow rate due to acceleration after the engine start).

In the case where exhaust flow rate and HC concentration peaks are well aligned (Fig. 7a-b), both OFRs report too low SOA emission, which was also the case in Fig. 1, but DOFR result is closer to the true one. However, when the two signals are misaligned (Fig. 7c-d), DOFR results in higher overestimation of the emitted SOA because the HC concentration is still elevated when the exhaust flow rate starts to increase. This is the case with PAM as well, but since the HC peak is distributed over a longer time period, the concentration is not as high as in DOFR and the resulting SOA emission agrees better with the true emission.

In Sect. 3.1, the performance of the OFRs was investigated only for one gasoline vehicle running two cycles, and DOFR typically resulted in better agreement with true SOA PF than PAM. However, as shown in Fig. 7, DOFR does not result in better agreement in all cases. Different vehicle types and more aggressive driving cycles may exhibit different behaviour in tailpipe gas concentrations and exhaust flow rate compared to the gasoline vehicle driving the NEDC, and also the alignment between the concentration peaks and the changes in exhaust flow rate may be different. For example, in Diesel vehicles the CO₂ concentration is load-dependent whereas in the gasoline vehicle studied here the tailpipe CO₂ concentration was almost constant. Hybrid vehicles may repeatedly switch the combustion engine off and on during the driving cycle.

Thus, to investigate the performance of the OFRs and data analysis methods in a broader range of instances, we performed a Monte Carlo analysis on synthetic driving cycles that include various different combinations of exhaust flow rate, CO₂ concentrations and HC concentrations.

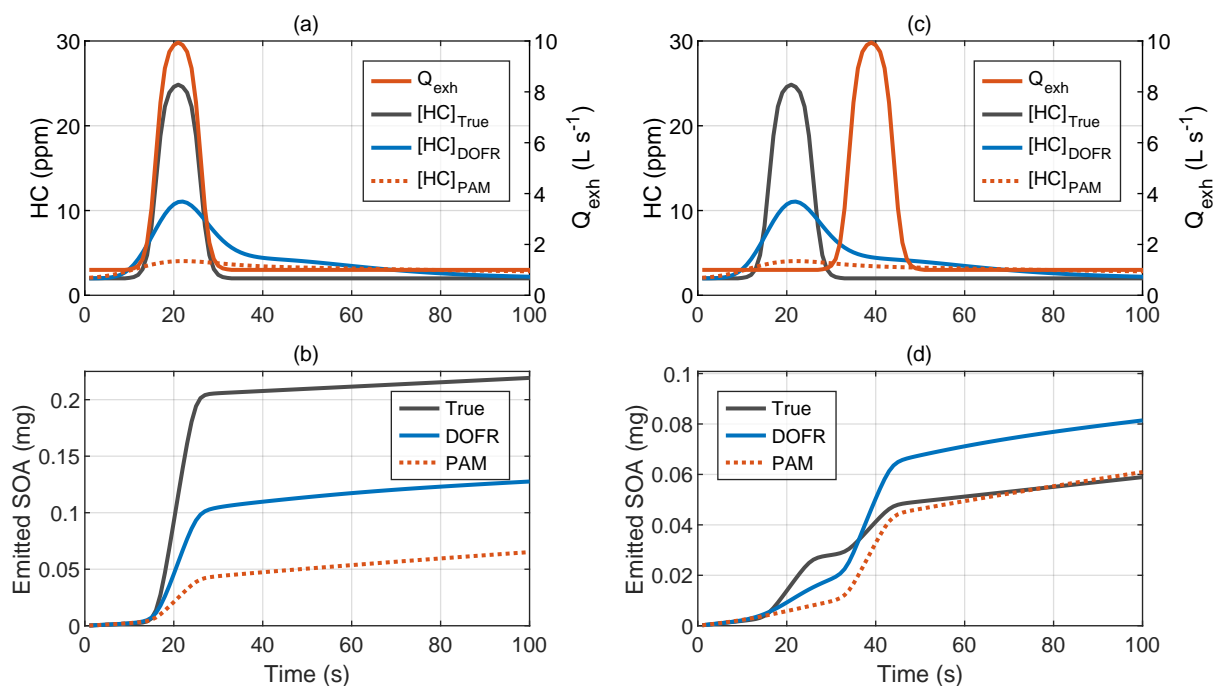


Figure 7. Two distinct example time series of exhaust gas concentrations and exhaust flow rate. In the typical acceleration case (a)-(b), the DOFR SOA emission is closer to true, whereas in the case where HC peak and exhaust flow rate peak are not aligned (c)-(d), the PAM outcome agrees better with true emission. It is assumed that the SOA formation is directly proportional to HC concentration.

3.3 Synthetic driving cycles

Driving cycles have three variables that affect the SOA PF: CO_2 concentration, HC concentration and exhaust flow rate. The synthetic driving cycles were generated by dividing the cycle in periods of random duration for each variable, where the value of the variable was random (but constant for the period duration). The periods for each variable were generated independently
 340 of each other, so that the changes in the values of each variable do not necessarily coincide with changes in the other two variables. The generation algorithm is described in more detail in Sect. S3 and examples of generated cycles are shown in Fig. S17. In total, 10000 synthetic driving cycles were generated.

Figures 8a-b show that the distribution of full cycle SOA PFs was skewed towards underestimation for both reactors, but more severely for PAM, when using the *standard* method for the synthetic driving cycles. The two other methods shown, the
 345 *OFR* CO_2 and *convolution* methods, agreed well with the true PF. Only three methods are shown here because it was already observed in Sect. 3.1.1 that the *averaging* method is not suitable for calculating the full cycle PFs, and that the *CVS* method always leads to correct full cycle PF. The *deconvolution* method was too time consuming to apply for all 10000 driving cycles.

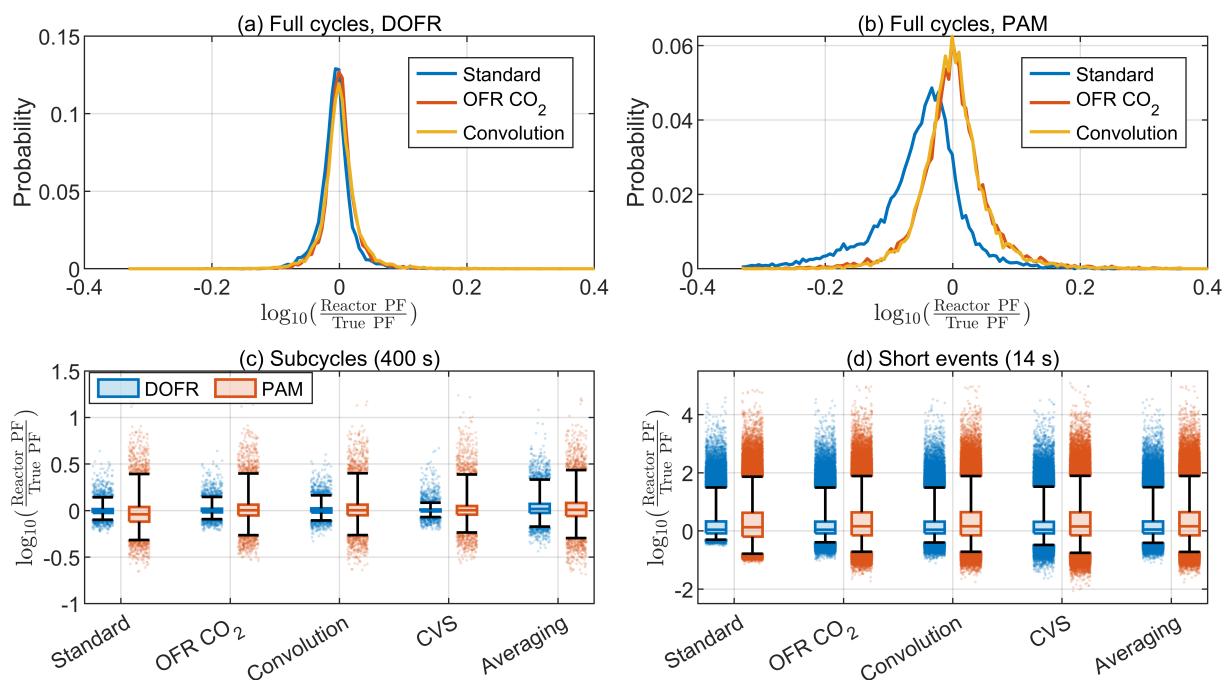


Figure 8. The probability distributions for full cycle SOA PFs for 10000 synthetic driving cycles using DOFR (a) and PAM (b), and the the deviation in OFR PFs for 400 s (c) and 14 s bins (d) in the synthetic driving cycles. Boxes represent 25th and 75th percentiles, and the line inside the box represents the median value. The points are considered outliers if they are greater than 99th percentile or lower than 1st percentile. The whiskers extend to most extreme data points that are not outliers.

Similar to full cycle PFs, the standard method typically underestimated the PF for PAM when calculating the PFs for 400 s subcycles (Fig. 8c). Among the other calculation methods, the *averaging* method led to broadest distribution of deviations and the *CVS* method performed best for both OFRs.

Because of the other disadvantages of the *CVS* sampling discussed in Sect. 3.1.1, the *OFR CO₂* and *convolution* methods seem most feasible for exhaust measurements based on the distributions in Fig. 8c. Using the *OFR CO₂* method for 400 s subcycles in the synthetic cycles, the median OFR-to-True ratio was 1.00 for DOFR and 1.01 for PAM. 50% of DOFR PF ratios ranged between 0.96 and 1.05 and PAM ratios between 0.89 and 1.16. 98% of DOFR PF ratios ranged between 0.81 and 1.40 and PAM ratios between 0.54 and 2.50.

Figure 8d shows that the different calculation methods resulted in very similar distributions when calculating the SOA PFs for short events. The *CVS* method led to most negative outliers for both OFRs, and the *standard* method least. The PAM median was closest to true value when using the *standard* method, but on the other hand the 25th percentile was more negative than with the other methods. In *OFR CO₂* method, 50% of DOFR PF ratios ranged between 0.82 and 2.09 and PAM ratios between 0.71 and 4.38. 98% of DOFR PF ratios ranged between 0.41 and 31.00 and PAM ratios between 0.19 and 77.26. A summary of deviations of OFR-derived PFs from the true values in both real cycles and synthetic cycles is shown in Table 1.



Table 1. Ratios of reactor PF to true PF when using OFR CO₂ method. For each case, the median ratio and 25th, 75th, 1st and 99th percentiles of ratios are shown (notation of P₂₅ for 25th percentile etc. is used).

		Subcycles (400 s)					Short events (14 s)				
		Median	P ₂₅	P ₇₅	P ₀₁	P ₉₉	Median	P ₂₅	P ₇₅	P ₀₁	P ₉₉
Real cycles	PAM	1.04	0.88	1.20	0.87	1.22	1.47	1.03	2.61	0.36	4.99
	DOFR	0.95	0.92	0.98	0.91	1.01	1.09	0.89	1.43	0.55	2.41
Synthetic cycles	PAM	1.01	0.89	1.16	0.54	2.50	1.45	0.71	4.38	0.19	77.26
	DOFR	1.00	0.96	1.05	0.81	1.40	1.11	0.82	2.09	0.41	31.00

Since a significant fraction of OFR-derived PFs were more than 10-fold compared to true PFs for short, 14 s segments, and the agreement was better for longer (400 s) segments, it is of interest to determine what is the minimum segment durations for which the OFR results are accurate enough. If we choose that the OFR result is acceptable when 99% of the PFs are less than three times the true PF, the minimum duration was 110 s for DOFR and 350 s for PAM. The deviations as a function of bin duration are shown in Fig. S12.

4 Conclusions

In this study, the effect of OFR transfer function on the accuracy of SOA PFs in transient driving cycles was investigated by using semi-synthetic and synthetic exhaust gas data. The analysis was done for two OFRs: a PAM reactor with a broad transfer function and DOFR with a narrower transfer function.

Even though the wide residence time distributions of OFRs resulted in momentary PFs that differed from the true PFs, it was possible to determine the integrated PFs relatively accurately for longer periods within the driving cycles. However, a wrong data analysis method could lead to PFs that were more than double of true PF.

When determining SOA PFs of short-duration events in a driving cycle, such as accelerations, the errors were larger for both OFRs compared to PFs of longer periods. The narrower transfer function of DOFR was advantageous, since the 1st and 99th percentiles of OFR-to-true PF ratios in the short-duration events (14 s periods) in real driving cycles were 0.55 and 2.41, respectively, for DOFR and 0.36 and 4.99 for PAM (using OFR CO₂ method).

When extending the study to synthetic driving cycles, the OFRs still reported the full cycle PFs with relatively small error. For 14 s bins in the synthetic driving cycles, it was observed that the OFRs may overestimate the SOA PFs by more than factor of ten. It is questionable whether any of the studied OFRs can be used to determine SOA PFs for that short driving events since the potential error is so high. At least, the uncertainty should be addressed when reporting the PFs. On the other hand, the synthetic driving cycles are random and do not necessarily represent typical driving cycles, so the results represent maximum possible error rather than typical error observed in real driving cycles. More real cycles should be studied in order to evaluate the potential error.



385 By lengthening the bin duration to 110 s, the 99th percentile of DOFR PF ratios was below 3 in the synthetic driving cycles. The 99th percentile of PAM PF ratios was below 3 when the bin duration was longer than 350 s.

Deconvolution of SOA concentration measured at OFR outlet seemed promising method because it enhanced the accuracy of SOA PFs significantly. However, the result was obtained by assuming noise-free measurement of mass concentration, and thus its applicability to real-world scenarios should be further studied.

390 There are also other reasons than the transfer function alone for OFRs to report incorrect SOA production factors, such as non-tropospheric gas chemistry or non-tropospheric losses (Peng and Jimenez, 2020, 2017; Peng et al., 2019; Palm et al., 2016). In this paper, we only studied the error that is caused by the OFR transfer function. Other sources of error were isolated by assuming that the oxidation in OFRs perfectly reproduces atmospheric oxidation and that there are no non-atmospheric losses in the OFRs. The analysis is limited to conditions where SOA formation potential is directly proportional to HC concentration
395 and where the proportionality is constant throughout the driving cycle.

Even though the assumption of SOA concentration being directly proportional to HC concentration does not generally hold, the HC measurement from tailpipe accompanied with the methods presented in this study is a good sensitivity test for transfer function -related uncertainties when determining the SOA PFs with an oxidation flow reactor. Similar analysis apply when using any other slow-response instrument to determine emission factors.

400 Arising from our analysis, we present the following best practise recommendations for OFR emission measurements:

- Before the start of the cycle, the reactor must be sampling zero air to avoid previous driving affecting the cycle SOA PF. The exhaust sampling must start at the same time as driving cycle starts. This concerns the engine-off periods of hybrid vehicles as well: zero air sampling should be started immediately when the combustion engine is switched off, and the tailpipe sampling started when the engine turns back on. When sampling from CVS, this is done automatically.
- 405 – When the cycle ends, the reactor must immediately start sampling zero air. The measurement must be continued at least for duration of the OFR τ_{peak} to make the delay correction in data after-treatment possible. When sampling from CVS (or when using the convolution method), the sampling of zero air must be continued at least for duration of OFR mean residence time, but longer sampling time will result in more accurate PF (Fig. S13).
- In order to use the OFR CO_2 method or convolution method, CO_2 should be measured downstream of the OFR, or
410 the OFR outlet CO_2 concentration should be simulated by convolving the tailpipe concentration with the OFR transfer function and dividing with the dilution ratio.
- When using other than *standard* or *deconvolution* method, the distance-based production factors should be calculated by first calculating the fuel-based production factor with one of the presented methods, and then using OBD data to convert the fuel-based PF to distance-based.

415 The Matlab code used in this study is available as a Supplement file to reproduce the analysis for any OFR with a known transfer function and for any driving cycle for which the CO_2 and HC concentrations and exhaust flow rate are available.



5 Methods

5.1 OFR characterization

Dekati oxidation flow reactor (DOFR) is a commercial oxidation flow reactor, which dimensions are very close to those of
420 Tampere secondary aerosol reactor (TSAR; Simonen et al. (2017)). The main geometrical additions compared to TSAR are
a conical outlet, a laminating grid element in the inlet and unlike TSAR, all sample is evacuated through a single outlet. The
oxidation reactor is surrounded by 12 UV lamps of which two can be switched on individually and the rest of the lamps in
pairs, whereas TSAR has two intensity-controlled UV lamps (Kuittinen et al., 2021a). The housing of the oxidation reactor is
cooled with air. The air cooling in the commercial version is enhanced compared to the prototype version used here. Similar to
425 TSAR, DOFR is an OFR254 type reactor, which means that OH radicals inside the reactor are generated by 254 nm UV light
from externally mixed ozone and water vapor.

The transfer function of DOFR was determined for CO₂ and toluene by injecting 10 s square pulses of gases into the reactor
and measuring them downstream of the reactor. The CO₂ was measured with LI-840 analyzer (LI-COR Inc.) and toluene with
Vocus proton transfer reaction mass spectrometer (Aerodyne Research Inc.). The gases were injected at the enclosure inlet and
430 CO₂ was measured directly downstream of the reactor while the toluene was measured downstream of ejector diluter, which
is an integral part of DOFR. Thus, the toluene RTD describes the response of the full unit, although we assume that this is the
case for CO₂ RTD as well because the residence time in the diluter and its sampling lines is minor. The mean flow rate through
DOFR was 6.8 lpm during the CO₂ experiments and 6.0 lpm during the toluene experiments.

The square pulses were generated by continuously injecting constant mass flow rate of CO₂ or N₂ mixed with toluene into
435 a fast pneumatic 3-way valve (MS-151-DA actuator with SS-42GXS6MM-51D 3-way valve; Swagelok Company), one outlet
connected to the DOFR inlet and the other to the excess line. The toluene vapor was generated with a permeation oven (V-OVG;
Owlstone Inc.). The measurement setup is shown in Fig. S1.

The DOFR RTDs of 10 s pulses were measured for 3 different UV lamp configurations: 'off', 'low' (two central UV
lamps on), and 'high' (all UV lamps on). The O₃ generation was switched off to prevent toluene reacting with OH radicals
440 when measuring the toluene RTD. The measured RTDs correspond to 10 s input pulses, so they do not represent the actual
transfer function which is the response to a Dirac delta input. Thus, the OFR transfer functions were determined by finding
the transfer function that resulted in best agreement with the measured concentration when convolving with 10 s square pulse.
The candidate function was a linear combination of Taylor distributions (Lambe et al., 2011; Huang and Seinfeld, 2019), and
the best fit was found with Matlab function '*fit*'. The gas analyzer response was not determined separately, so it is included
445 in the reported transfer functions. In this study, the transfer function corresponding to 'low' UV lamp configuration was used
to simulate the DOFR output. This lamp configuration resulted in OH exposure of $7.9 \cdot 10^{11} \text{ cm}^{-3}\text{s}^{-1}$ according to toluene
measurements. The DOFR transfer functions for CO₂ and toluene are shown in Fig. S4, and the comparisons between the
convolved square pulses and the measured DOFR output concentrations are shown in Figs. S5 and S6.

By switching the O₃ reactor on, we also measured the mass concentration that was produced from 10 s toluene pulse for
450 the 'low' UV lamp configuration. The mass concentration was measured with an electrical low-pressure impactor (ELPI,



Dekati Ltd.; Keskinen et al. (1992)) with improved nanoparticle resolution (Yli-Ojanperä et al., 2010). It would be possible to determine a transfer function for SOA formation based on these measurements, but since such data was not available for PAM chamber, we simulated the SOA formation in both OFRs by assuming that the SOA formation response is equal to CO₂ response. Simonen et al. (2017) did measure the PAM SOA formation for a toluene pulse, but in those measurements the PAM ring flow was not used. Since the usage of ring flow is a standard method in PAM measurements and affects the transfer function, we used the CO₂ pulse data measured by Lambe et al. (2011) to determine the PAM transfer function by the same fitting procedure as for the DOFR (Fig. S7). In the measurements by Lambe et al. (2011), PAM ring flow was used and the UV lamps were on. Using the CO₂ transfer function to simulate the SOA formation in DOFR resulted in a satisfactory agreement with the experimental data (Fig. S8), so the usage of CO₂ transfer function in this study is justified.

460 For the OFR delay correction (Eq. 7) we used the peak residence time as the correction constant. The peak residence time (τ_{peak}) is the residence time for maximum value in the transfer function (i.e., $E(\tau_{peak}) = \max(E(t))$). Figure S10 shows that the error in SOA PF was smallest when the delay correction constant was close to τ_{peak} .

5.2 Vehicle exhaust measurements

The vehicle in real driving cycle measurements was a Euro 6 gasoline vehicle equipped with 1.4 l turbocharged direct injection engine (110 kW). The vehicle was soaked for 15 h before the cold-start cycle and pre-conditioned by driving at 80 kmh⁻¹ for 5 min before the hot-start cycle. The hot start cycle started with idling engine. In the simulations, it was assumed that the OFRs are flushed with zero air until the cycle starts and immediately after the cycle ends. So even though engine is running before the start of hot-start NEDC, the OFRs are filled with zero air at $t = 0$ s.

The total hydrocarbon concentration (methane equivalent ppm) was measured with a flame ionization detector and the CO₂ concentration with a non-dispersive infrared analyzer. Both gases were sampled directly from tailpipe. The exhaust mass flow rate was calculated based on the intake air flow rate and fuel consumption obtained from the on-board diagnostics data. The fuel carbon content (k') of 860 g kg⁻¹ was used in the calculations.

Code and data availability. The engine exhaust data for the real driving cycles is available in the Supplement. The Matlab code to reproduce the analysis is available in the Supplement.

475 *Author contributions.* P.S.: Original idea, data processing, writing the manuscript, planning and execution of experiments. M.D.M.: Manuscript conceptualisation and preparation. P.P.: DOFR experiments, Vocus data processing, commenting the manuscript. A.H., A.K.: DOFR experiments, commenting the manuscript. P.M.: Planning of chassis dynamometer experiments and commenting manuscript. P.K.: Project management, planning and execution of chassis dynamometer experiments and commenting manuscript. J.K.: Funding, project management, manuscript conceptualization and preparation.



480 *Competing interests.* J.K. is a member of the board of Dekati Ltd.

Acknowledgements. The chassis dynamometer measurements were conducted within Health relevant and energy efficient regulation of exhaust particle emissions (HERE) project [decision number 40330/13] funded by Business Finland (Tekes). We acknowledge additional funding from the Academy (now: Research council) of Finland's Flagship programme (decision No.'s 337551, 357903) and infrastructure funding (decision No.'s 328823, 345528). We acknowledge the engine laboratory personnel at Dinex Finland Oy for the chassis dynamometer
485 measurements and Dekati Ltd for providing a DOFR prototype for testing.



References

- Ajtay, D. and Weilenmann, M.: Compensation of the exhaust gas transport dynamics for accurate instantaneous emission measurements, *Environmental science & technology*, 38, 5141–5148, 2004.
- Conesa, J. A.: *Chemical Reactor Design - Mathematical Modeling and Applications*, John Wiley & Sons, 2020.
- 490 Fogler, H.: *Elements of Chemical Reaction Engineering*, Elements of Chemical Reaction Engineering, Prentice Hall PTR, 2006.
- Franco, V.: Evaluation and improvement of road vehicle pollutant emission factors based on instantaneous emissions data processing, Ph.D. thesis, Universitat Jaume I, available at <http://hdl.handle.net/10803/146187>, 2014.
- Ganesan, B. and Clark, N. N.: Relationships Between Instantaneous and Measured Emissions in Heavy Duty Applications, *SAE Transactions*, 110, 1798–1806, 2001.
- 495 Geivanidis, S. and Samaras, Z.: Development of a dynamic model for the reconstruction of tailpipe emissions from measurements on a constant volume sampling dilution system, *Measurement Science and Technology*, 19, 015 404, 2007.
- Giechaskiel, B., Lähde, T., Melas, A. D., Valverde, V., and Clairotte, M.: Uncertainty of laboratory and portable solid particle number systems for regulatory measurements of vehicle emissions, *Environmental Research*, 197, 111 068, 2021.
- Gordon, T. D., Presto, A. A., May, A. A., Nguyen, N. T., Lipsky, E. M., Donahue, N. M., Gutierrez, A., Zhang, M., Maddox, C., Rieger, P.,
500 Chattopadhyay, S., Maldonado, H., Maricq, M. M., and Robinson, A. L.: Secondary organic aerosol formation exceeds primary particulate matter emissions for light-duty gasoline vehicles, *Atmospheric Chemistry and Physics*, 14, 4661–4678, <https://doi.org/10.5194/acp-14-4661-2014>, 2014a.
- Gordon, T. D., Presto, A. A., Nguyen, N. T., Robertson, W. H., Na, K., Sahay, K. N., Zhang, M., Maddox, C., Rieger, P., Chattopadhyay, S., Maldonado, H., Maricq, M. M., and Robinson, A. L.: Secondary organic aerosol production from diesel vehicle exhaust: impact of
505 aftertreatment, fuel chemistry and driving cycle, *Atmospheric Chemistry and Physics*, 14, 4643–4659, <https://doi.org/10.5194/acp-14-4643-2014>, 2014b.
- Hallquist, M., Wenger, J. C., Baltensperger, U., Rudich, Y., Simpson, D., Claeys, M., Dommen, J., Donahue, N. M., George, C., Goldstein, A. H., Hamilton, J. F., Herrmann, H., Hoffmann, T., Iinuma, Y., Jang, M., Jenkin, M. E., Jimenez, J. L., Kiendler-Scharr, A., Maenhaut, W., McFiggans, G., Mentel, T. F., Monod, A., Prévôt, A. S. H., Seinfeld, J. H., Surratt, J. D., Szmigielski, R., and Wildt, J.: The formation, properties and impact of secondary organic aerosol: current and emerging issues, *Atmospheric Chemistry and Physics*, 9, 5155–5236, <https://doi.org/10.5194/acp-9-5155-2009>, 2009.
- 510 Hawley, J. G., Brace, C. J., Cox, A., Ketcher, D., and Stark, R.: Influence of Time-Alignment on the Calculation of Mass Emissions on a Chassis Rolls Dynamometer, in: *SAE 2003 World Congress & Exhibition*, SAE International, <https://doi.org/10.4271/2003-01-0395>, 2003.
- 515 Huang, Y. and Seinfeld, J. H.: A note on flow behavior in axially-dispersed plug flow reactors with step input of tracer, *Atmospheric Environment: X*, 1, 100 006, <https://doi.org/10.1016/j.aeaoa.2019.100006>, 2019.
- Kanakidou, M., Seinfeld, J. H., Pandis, S. N., Barnes, I., Dentener, F. J., Facchini, M. C., Van Dingenen, R., Ervens, B., Nenes, A., Nielsen, C. J., Swietlicki, E., Putaud, J. P., Balkanski, Y., Fuzzi, S., Horth, J., Moortgat, G. K., Winterhalter, R., Myhre, C. E. L., Tsigaridis, K., Vignati, E., Stephanou, E. G., and Wilson, J.: Organic aerosol and global climate modelling: a review, *Atmospheric Chemistry and
520 Physics*, 5, 1053–1123, <https://doi.org/10.5194/acp-5-1053-2005>, 2005.
- Karjalainen, P., Timonen, H., Saukko, E., Kuuluvainen, H., Saarikoski, S., Aakko-Saksa, P., Murtonen, T., Bloss, M., Dal Maso, M., Simonen, P., Ahlberg, E., Svenningsson, B., Brune, W. H., Hillamo, R., Keskinen, J., and Rönkkö, T.: Time-resolved characterization of primary



- particle emissions and secondary particle formation from a modern gasoline passenger car, *Atmospheric Chemistry and Physics*, 16, 8559–8570, <https://doi.org/10.5194/acp-16-8559-2016>, 2016.
- 525 Keskinen, J., Pietarinen, K., and Lehtimäki, M.: Electrical low pressure impactor, *Journal of Aerosol Science*, 23, 353–360, 1992.
- Kuittinen, N., McCaffery, C., Peng, W., Zimmerman, S., Roth, P., Simonen, P., Karjalainen, P., Keskinen, J., Cocker, D. R., Durbin, T. D., Rönkkö, T., Bahreini, R., and Karavalakis, G.: Effects of driving conditions on secondary aerosol formation from a GDI vehicle using an oxidation flow reactor, *Environmental Pollution*, 282, 117 069, <https://doi.org/https://doi.org/10.1016/j.envpol.2021.117069>, 2021a.
- 530 Kuittinen, N., McCaffery, C., Zimmerman, S., Bahreini, R., Simonen, P., Karjalainen, P., Keskinen, J., Rönkkö, T., and Karavalakis, G.: Using an oxidation flow reactor to understand the effects of gasoline aromatics and ethanol levels on secondary aerosol formation, *Environmental Research*, 200, 111 453, <https://doi.org/https://doi.org/10.1016/j.envres.2021.111453>, 2021b.
- Lambe, A. T., Ahern, A. T., Williams, L. R., Slowik, J. G., Wong, J. P. S., Abbatt, J. P. D., Brune, W. H., Ng, N. L., Wright, J. P., Croasdale, D. R., Worsnop, D. R., Davidovits, P., and Onasch, T. B.: Characterization of aerosol photooxidation flow reactors: heterogeneous oxidation, secondary organic aerosol formation and cloud condensation nuclei activity measurements, *Atmospheric Measurement Techniques*, 4, 445–461, <https://doi.org/10.5194/amt-4-445-2011>, 2011.
- 535 Madireddy, M. and Clark, N.: Sequential inversion technique and differential coefficient approach for accurate instantaneous emissions measurement, *International Journal of Engine Research*, 7, 437–446, 2006.
- Mahadevan, V., Iyer, S., and Klinikowski, D.: Recovery of tail pipe species concentrations and its effect on emissions calculations from raw exhaust gas streams during chassis dynamometer tests, *SAE International Journal of Engines*, 9, 1763–1774, 2016.
- 540 Nault, B. A., Jo, D. S., McDonald, B. C., Campuzano-Jost, P., Day, D. A., Hu, W., Schroder, J. C., Allan, J., Blake, D. R., Canagaratna, M. R., Coe, H., Coggon, M. M., DeCarlo, P. F., Diskin, G. S., Dunmore, R., Flocke, F., Fried, A., Gilman, J. B., Gkatzelis, G., Hamilton, J. F., Hanisco, T. F., Hayes, P. L., Henze, D. K., Hodzic, A., Hopkins, J., Hu, M., Huey, L. G., Jobson, B. T., Kuster, W. C., Lewis, A., Li, M., Liao, J., Nawaz, M. O., Pollack, I. B., Peischl, J., Rappenglück, B., Reeves, C. E., Richter, D., Roberts, J. M., Ryerson, T. B., Shao, M., Sommers, J. M., Walega, J., Warneke, C., Weibring, P., Wolfe, G. M., Young, D. E., Yuan, B., Zhang, Q., de Gouw, J. A., and Jimenez, J. L.: Secondary organic aerosols from anthropogenic volatile organic compounds contribute substantially to air pollution mortality, *Atmospheric Chemistry and Physics*, 21, 11 201–11 224, <https://doi.org/10.5194/acp-21-11201-2021>, 2021.
- 545 Palm, B. B., Campuzano-Jost, P., Ortega, A. M., Day, D. A., Kaser, L., Jud, W., Karl, T., Hansel, A., Hunter, J. F., Cross, E. S., Kroll, J. H., Peng, Z., Brune, W. H., and Jimenez, J. L.: In situ secondary organic aerosol formation from ambient pine forest air using an oxidation flow reactor, *Atmospheric Chemistry and Physics*, 16, 2943–2970, <https://doi.org/10.5194/acp-16-2943-2016>, 2016.
- 550 Park, G., Kim, K., Park, T., Kang, S., Ban, J., Choi, S., Yu, D.-G., Lee, S., Lim, Y., Kim, S., Mun, S., Woo, J.-H., Jeon, C.-S., and Lee, T.: Primary and secondary aerosols in small passenger vehicle emissions: Evaluation of engine technology, driving conditions, and regulatory standards, *Environmental Pollution*, 286, 117 195, <https://doi.org/https://doi.org/10.1016/j.envpol.2021.117195>, 2021.
- Peng, Z. and Jimenez, J. L.: Modeling of the chemistry in oxidation flow reactors with high initial NO, *Atmospheric Chemistry and Physics*, 17, 11 991–12 010, <https://doi.org/10.5194/acp-17-11991-2017>, 2017.
- 555 Peng, Z. and Jimenez, J. L.: Radical chemistry in oxidation flow reactors for atmospheric chemistry research, *Chemical Society Reviews*, 49, 2570–2616, <https://doi.org/10.1039/C9CS00766K>, 2020.
- Peng, Z., Lee-Taylor, J., Orlando, J. J., Tyndall, G. S., and Jimenez, J. L.: Organic peroxy radical chemistry in oxidation flow reactors and environmental chambers and their atmospheric relevance, *Atmospheric Chemistry and Physics*, 19, 813–834, <https://doi.org/10.5194/acp-19-813-2019>, 2019.



- 560 Pieber, S. M., Kumar, N. K., Klein, F., Comte, P., Bhattu, D., Dommen, J., Bruns, E. A., Kılıç, D., El Haddad, I., Keller, A., Czerwinski, J., Heeb, N., Baltensperger, U., Slowik, J. G., and Prévôt, A. S. H.: Gas-phase composition and secondary organic aerosol formation from standard and particle filter-retrofitted gasoline direct injection vehicles investigated in a batch and flow reactor, *Atmospheric Chemistry and Physics*, 18, 9929–9954, <https://doi.org/10.5194/acp-18-9929-2018>, 2018.
- Platt, S. M., El Haddad, I., Zardini, A. A., Clairotte, M., Astorga, C., Wolf, R., Slowik, J. G., Temime-Roussel, B., Marchand, N., Ježek, 565 I., Drinovec, L., Močnik, G., Möhler, O., Richter, R., Barmet, P., Bianchi, F., Baltensperger, U., and Prévôt, A. S. H.: Secondary organic aerosol formation from gasoline vehicle emissions in a new mobile environmental reaction chamber, *Atmospheric Chemistry and Physics*, 13, 9141–9158, <https://doi.org/10.5194/acp-13-9141-2013>, 2013.
- Pöschl, U.: *Atmospheric Aerosols: Composition, Transformation, Climate and Health Effects*, *Angewandte Chemie International Edition*, 44, 7520–7540, <https://doi.org/https://doi.org/10.1002/anie.200501122>, 2005.
- 570 Roth, P., Yang, J., Stamatis, C., Barsanti, K. C., Cocker, D. R., Durbin, T. D., Asa-Awuku, A., and Karavalakis, G.: Evaluating the relationships between aromatic and ethanol levels in gasoline on secondary aerosol formation from a gasoline direct injection vehicle, *Science of The Total Environment*, 737, 140 333, <https://doi.org/https://doi.org/10.1016/j.scitotenv.2020.140333>, 2020.
- Seinfeld, J. H. and Pandis, S. N.: *Atmospheric chemistry and physics : from air pollution to climate change*, Wiley, Hoboken (N.J.), 2nd edn., 2006.
- 575 Simonen, P., Saukko, E., Karjalainen, P., Timonen, H., Bloss, M., Aakko-Saksa, P., Rönkkö, T., Keskinen, J., and Dal Maso, M.: A new oxidation flow reactor for measuring secondary aerosol formation of rapidly changing emission sources, *Atmospheric Measurement Techniques*, 10, 1519–1537, <https://doi.org/10.5194/amt-10-1519-2017>, 2017.
- Simonen, P., Kalliokoski, J., Karjalainen, P., Rönkkö, T., Timonen, H., Saarikoski, S., Aurela, M., Bloss, M., Triantafyllopoulos, G., Kontses, A., Amanatidis, S., Dimaratos, A., Samaras, Z., Keskinen, J., Dal Maso, M., and Ntziachristos, L.: Characterization of laboratory and real 580 driving emissions of individual Euro 6 light-duty vehicles – Fresh particles and secondary aerosol formation, *Environmental Pollution*, 255, 113 175, <https://doi.org/https://doi.org/10.1016/j.envpol.2019.113175>, 2019.
- Timonen, H., Karjalainen, P., Saukko, E., Saarikoski, S., Aakko-Saksa, P., Simonen, P., Murtonen, T., Dal Maso, M., Kuuluvainen, H., Bloss, M., Ahlberg, E., Svenningsson, B., Pagels, J., Brune, W. H., Keskinen, J., Worsnop, D. R., Hillamo, R., and Rönkkö, T.: Influence of fuel ethanol content on primary emissions and secondary aerosol formation potential for a modern flex-fuel gasoline vehicle, *Atmospheric 585 Chemistry and Physics*, 17, 5311–5329, <https://doi.org/10.5194/acp-17-5311-2017>, 2017.
- Weilenmann, M., Soltic, P., and Ajtay, D.: Describing and compensating gas transport dynamics for accurate instantaneous emission measurement, *Atmospheric Environment*, 37, 5137–5145, <https://doi.org/https://doi.org/10.1016/j.atmosenv.2003.05.004>, 11th International Symposium, Transport and Air Pollution, 2003.
- Weisstein, E. W.: "Convolution." From MathWorld—A Wolfram Web Resource, <https://mathworld.wolfram.com/Convolution.html>, [Online; 590 accessed 28-June-2023], 2023.
- Yli-Ojanperä, J., Kannosto, J., Marjamäki, M., and Keskinen, J.: Improving the nanoparticle resolution of the ELPI, *Aerosol and Air Quality Research*, 10, 360–366, 2010.
- Zhang, J., Peng, J., Song, A., Lv, Z., Tong, H., Du, Z., Guo, J., Wu, L., Wang, T., Hallquist, M., et al.: Marked impacts of transient conditions on potential secondary organic aerosol production during rapid oxidation of gasoline exhausts, *npj Climate and Atmospheric Science*, 6, 595 59, 2023.
- Zhang, Q., Jimenez, J. L., Canagaratna, M. R., Allan, J. D., Coe, H., Ulbrich, I., Alfarra, M. R., Takami, A., Middlebrook, A. M., Sun, Y. L., Dzepina, K., Dunlea, E., Docherty, K., DeCarlo, P. F., Salcedo, D., Onasch, T., Jayne, J. T., Miyoshi, T., Shimono, A.,



- 600 Hatakeyama, S., Takegawa, N., Kondo, Y., Schneider, J., Drewnick, F., Borrmann, S., Weimer, S., Demerjian, K., Williams, P., Bower, K., Bahreini, R., Cottrell, L., Griffin, R. J., Rautiainen, J., Sun, J. Y., Zhang, Y. M., and Worsnop, D. R.: Ubiquity and dominance of oxygenated species in organic aerosols in anthropogenically-influenced Northern Hemisphere midlatitudes, *Geophysical Research Letters*, 34, <https://doi.org/https://doi.org/10.1029/2007GL029979>, 2007.
- Zhao, Y., Lambe, A. T., Saleh, R., Saliba, G., and Robinson, A. L.: Secondary organic aerosol production from gasoline vehicle exhaust: effects of engine technology, cold start, and emission certification standard, *Environmental science & technology*, 52, 1253–1261, <https://doi.org/10.1021/acs.est.7b05045>, 2018.